

Observation of Persistent Zero Modes and Superconducting Vortex Doublets in UTe₂

Nileema Sharma^{1,2†}, Matthew Toole^{1,2†}, James McKenzie^{1,2}, Fangjun Cheng^{1,2}, Mitchell M. Bordelon³, Sean M. Thomas³, Priscila F. S. Rosa³, Yi-Ting Hsu^{1*}, and Xiaolong Liu^{1,2*}

¹*Department of Physics and Astronomy, University of Notre Dame, Notre Dame, IN 46556, USA*

²*Stavropoulos Center for Complex Quantum Matter, University of Notre Dame, Notre Dame, IN 46556, USA*

³*Los Alamos National Laboratory, Los Alamos, New Mexico 87545, USA*

* Corresponding authors. Email: yhsu2@nd.edu, xliu33@nd.edu

† These authors contributed equally to this work.

Abstract

Superconducting vortices can reveal electron pairing details and nucleate topologically protected states¹. Yet, vortices of bulk spin-triplet superconductors have never been visualized at the atomic scale. Recently, UTe₂ has emerged as a prime spin-triplet superconductor^{2,3,4,5,6,7,8}, but its superconducting order parameter is elusive, and whether time-reversal symmetry (TRS) is broken remains unsettled^{4,5,9,10}. Here, we visualize vortices on the (011) surface of ultra-clean UTe₂ single crystals^{11,12} ($T_c = 2.1$ K) using scanning tunneling microscopy (STM). We introduce $\frac{d^2I}{dV^2}$ imaging as an effective technique for vortex visualization in superconductors with substantial residual zero-energy density of states (DOS), as in UTe₂. Anisotropic single-flux-quantum vortices, with coherence lengths of ~ 12 nm (4 nm) parallel (perpendicular) to the **a**-axis, form a triangular vortex lattice (VL) under a small out-of-plane magnetic field. The invariance of vortex structures and VL under changes of field polarity and cooling history strongly supports time-reversal invariant superconductivity under zero field. At vortex cores (VCs), non-split, spectrally sharp zero-bias conductance peaks (ZBPs) persist up to 8 T that are consistent with symmetry-protected Majorana zero modes (MZMs) in a topological vortex line. Close examination of vortex structures reveals a mirror-asymmetric doublet—one with ZBPs and another with an enhanced superconducting gap, possibly originating from a field-induced multi-component order parameter.

Main

Topological superconductivity enables fault-tolerant quantum computation by hosting topologically protected non-Abelian anyons, known as Majorana modes^{13,14,15}, which emerge at the boundaries and defects of odd-parity superconductors with spin-triplet pairing^{16,17}. Compared to proximitized topological insulators^{18,19,20,21}, semiconductors¹⁷, or magnetic materials^{22,23,24,25}, a bulk Cooper-pair condensate with intrinsic spin-triplet pairing is extremely rare. The superconducting order parameter Δ of a spin-triplet condensate is represented using the \mathbf{d} vector, $\Delta(\mathbf{k}) \equiv (\mathbf{d} \cdot \boldsymbol{\sigma})i\sigma_2$, such that

$$\Delta = \begin{pmatrix} \Delta_{\uparrow\uparrow} & \Delta_{\uparrow\downarrow} \\ \Delta_{\downarrow\uparrow} & \Delta_{\downarrow\downarrow} \end{pmatrix} = \begin{pmatrix} -d_x + id_y & d_z \\ d_z & d_x + id_y \end{pmatrix} \quad (1)$$

where σ_i are the Pauli matrices. When vortices form in a spin-triplet condensate, the degrees of freedom from finite orbital ($L = 1$) and spin angular momenta ($S = 1$) can give rise to internal vortex structures and quantum phase winding that depart from that of conventional Abrikosov vortices in a spin-singlet superconductor²⁶. This is epitomized in superfluid ^3He with at least seven types of vortices²⁷. While such vortices of in ^3He have been probed spectroscopically via nuclear magnetic resonance^{27,28}, atomic scale visualization of vortices and their bound states in a charged spin-triplet superfluid has not been possible.

Recently, the heavy-fermion metal UTe_2 has been identified as a spin-triplet superconductor based on strong evidence including an abnormally large upper critical field^{8,11}, direction-dependent Knight shift²⁹, and magnetic field boosted superconductivity^{8,30}. As an orthorhombic crystal (Fig. 1a), UTe_2 has a D_{2h} point group symmetry allowing four irreducible representations (irreps), A_u , B_{1u} , B_{2u} , and B_{3u} , for odd-parity pairing³¹. Most intriguingly, signatures of time-reversal symmetry breaking (TRSB) were observed from edge-asymmetric tunneling spectra⁵, a nonzero polar Kerr effect^{4,32}, and two superconducting transitions⁴ in crystals with $T_c \approx 1.6$ K and residual resistivity ratios (RRRs) around 40. However, the highest quality UTe_2 crystals, synthesized via a molten-salt-flux technique¹², display a single superconducting transition and no sign of TRSB^{9,10}. Consequently, efforts towards understanding the microscopic details of superconductivity in UTe_2 have been hindered by inconsistent experimental results. In this report, we use ultra-clean UTe_2 single crystals with $T_c = 2.1$ K and $\text{RRR} \approx 680$ (Extended Data Fig. 1) to explore the intrinsic vortex properties of UTe_2 .

Vortex visualization via d^2I/dV^2 imaging

UTe_2 single crystals have an easy-cleave plane of (011) and a mirror plane perpendicular to the crystallographic \mathbf{a} -axis (Fig. 1a). A typical STM topographic image (Fig. 1b) reveals atomic chains of Te running along the \mathbf{a} -axis. We have further defined an in-plane \mathbf{b}^* -axis along the [01-1] direction perpendicular to \mathbf{a} . To introduce vortices, a magnetic field B is applied perpendicular

to the (011) surface, of which the normal direction is denoted as $\hat{\mathbf{n}}_{011}$. Under $B = 4$ T, which is significantly smaller than $H_{c2} \approx 20$ T (ref. 11), the superconducting gap ($|\Delta| \approx 270 - 300$ μeV) far away from vortices (Fig. 1c) remains almost unaltered (or slightly enhanced) from its zero-field value (Extended Data Fig. 2) and is slightly larger than that (~ 250 μeV)^{5,7,31} in UTe_2 with $T_c \approx 1.6$ K. Similar to previous reports, the gap is filled with considerable residual DOS that is spatially nonuniform at $B = 0$ T (Extended Data Fig. 2). As a result, although vortices typically have higher zero-bias differential conductance [$g(\mathbf{r}, V) \equiv dI/dV$] (Fig. 1c) due to vortex bound states, conventional vortex visualization via $g(\mathbf{r}, 0$ V) and $g(\mathbf{r}, \pm|\Delta|/e \approx \pm 300$ $\mu\text{V})$ imaging is hindered by the heterogeneous in-gap states and yields vortex images with compromised signal-to-noise ratios (Fig. 1d, under 4 T). Nonetheless, the effect of background DOS can be drastically suppressed via $dg/dV(\mathbf{r}, V)$ imaging at $V \approx \pm|\Delta|/2e$ (Fig. 1c). Indeed, a triangular lattice of highly elliptical vortices (indicated by black ellipses) is clearly resolved in the simultaneously acquired $dg/dV(\mathbf{r}, \pm 150$ $\mu\text{V})$ in Fig. 1e with inter-vortex distance d , while $dg/dV(\mathbf{r}, 0$ V) has minimal contrast, as expected.

Time-reversal invariant superconductivity under zero magnetic field

We now turn to the debated question of whether UTe_2 has a spontaneous TRSB superconducting order parameter (OP). A TRSB state necessarily requires a linear combination of two D_{2h} order parameters with a $\pi/2$ phase difference, e.g., $A_u \pm iB_{1u}$, yielding two degenerate ground states Δ_{\pm} with opposite chiralities under zero magnetic field^{33,34,35}. Such degeneracy is lifted under a magnetic field, making the two chiral states physically distinct. For a vortex, four combinations of chirality (C) and vorticity (V) (i.e., defined by the supercurrent winding direction, which is determined by the external magnetic field) are possible, $(C, V) = (+ +), (+ -), (- +),$ or $(- -)$, while each time-reversed pair is equivalent [e.g., $(+ -)$ and $(- +)$]. Therefore, depending on the combination of vorticity (determined by the field direction) and chirality of the ground state condensate (determined by state preparation), two types of vortices can be expected, each composed of distinct dominant and sub-dominant components with opposite chiralities^{33,34,35}. Hence, compared to polar Kerr measurements, wherein the signal might originate from remanent magnetization from trapped vortices upon field-cooling (FC)³², vortex imaging at the atomic scale constitutes a direct and unambiguous examination of TRS.

Assuming a spontaneous TRSB OP, we first perform FC of UTe_2 to 0.3 K under $B = 8.8$ T, preparing the system into a hypothetical $(+ +)$ state. The magnetic field is decreased to zero, through the Meissner state, inverted to -8.8 T, and cycled back to 8.8 T. At each stage, vortices are imaged in the same field of view (FOV) as shown in Fig. 2a. It is worth noting that if the ground state of a condensate is prepared to have a certain chirality, flipping the direction of the magnetic field below H_{c2} (i.e., changing vorticity) will not change its chirality as there is no

continuous symmetry connecting the states³³. Therefore, the vortices under positive and negative magnetic fields should correspond to (+ +) and (+ -) configurations with different vortex structures that are discernable even considering finite imaging temperatures³⁶. However, the lack of detectable differences between vortices and VLs in Fig. 2a under opposite magnetic fields suggest the absence of spontaneous TRSB. This is further supported by comparing the areal integrated $g(\mathbf{r}, 0 \text{ V})$ (Extended Data Fig. 3) between opposite magnetic fields in Fig. 2b that are expected to differ in a chiral superconductor^{34,37}, yet the differences are smaller than 0.3% for both $|B| = 4$ and 8 T. Next, instead of varying vorticity, we prepared the condensate into two hypothetically different chiralities by FC under ± 8.8 T and imaged the vortices under a series of positive magnetic fields (i.e., same vorticity) in the same FOV. While the vortices should correspond to (+ +) and (- +) configurations with different vortex structures and consequently VLs, triangular VLs with consistent inter-vortex distances d and vortex structures without statistically significant differences are observed at all magnetic fields for the two cases (Extended Data Fig. 4). Those observations therefore strongly suggest a time-reversal invariant OP in UTe_2 under zero magnetic field.

Under a finite magnetic field, on the other hand, multi-component superconductivity is often induced^{38,39,40,41,42}. This happens when the crystalline symmetry group of the system is lowered to a subgroup due to the breaking of spin-dependent symmetries, such as mirror reflections and rotations, by the Zeeman splitting. This field-induced symmetry reduction naturally allows the mixing of OPs from different irreps of the original point group. Such a scenario has been discussed in the context of UTe_2 ^{38,39}. Furthermore, experimental evidence of continuous \mathbf{d} -vector rotation^{43,44} and field-trainable Kerr effects¹⁰ in UTe_2 are consistent with a field-induced multi-component OP. In our case, the magnetic field is applied along $\hat{\mathbf{n}}_{011}$, which is neither parallel to a rotation axis nor perpendicular to a mirror plane. The resulting Zeeman splitting breaks all the rotation and mirror symmetries in UTe_2 's zero-field point group D_{2h} , preserving only the inversion symmetry. Because the point group is lowered from D_{2h} to C_i , the OP can be a mixture of all odd-parity irreps (A_u , B_{1u} , B_{2u} , and B_{3u}), where the specific coefficients depend on energetics. Consequently, with a magnetic field applied along the $\hat{\mathbf{n}}_{011}$ direction, we expect a field-induced multi-component OP in UTe_2 with either (1) preserved or (2) broken TRS. Note that our observation of a single type of vortices under different field polarities and cooling history (Fig. 2) is consistent with both possibilities: it does not rule out the possibility of a field-induced chiral OP, where the TRS is explicitly broken by the field. In contrast to a spontaneous TRSB superconductor under zero field, of which the chirality is not tied to the field direction, the chirality of a field-induced chiral OP is dictated to follow the direction of the magnetic field. Therefore, the vorticity and chirality of a superconducting vortex will always have the same sign [i.e., $(C, V) = (+ +)$ or $(- -)$], leading to only one type of vortices that is in agreement with experimental observations (Fig. 2).

Vortex core bound states

Because the vortices of UTe_2 form a triangular lattice, the magnetic flux enclosed by each vortex can be determined by measuring the inter-vortex distance. The result shown in Fig. 2c with both field polarities is in close agreement with single-flux-quantum vortices ($d \approx 1.07\sqrt{\Phi_0/B}$ for triangular lattice, where Φ_0 is flux quantum). In conventional vortices, non-topological Fermionic excitations known as Caroli-de Gennes-Matricon (CdGM) states have a low-energy spectrum of $E_n = \frac{|\Delta|^2}{E_F} \frac{(2n+1)}{2}$, where n is an integer and E_F is the Fermi energy¹⁹. Figures 3a and b show the normalized differential conductance spectra $g(V)/g(-520 \mu\text{V})$ taken at various fields on and off VCs, respectively. A pronounced ZBP with a full width at half maximum (FWHM) of $\sim 250 \mu\text{V}$ is observed at low fields (red double arrows; we have taken the residual in-gap DOS as a constant background), and gets gradually broadened as the field is increased further. Such FWHM is slightly smaller than those of ZBPs interpreted as MZMs^{19,45} in the vortices of $\text{FeTe}_{0.55}\text{Se}_{0.45}$. Surprisingly, the ZBPs in the VCs of UTe_2 persist up to 8 T (Extended Data Fig. 5), exceeding the Pauli paramagnetic limit of UTe_2 $H_P = 1.86T_c \approx 3.9$ T. Although discrete CdGM states with an energy separation of $\frac{|\Delta|^2}{E_F} \approx 14 \mu\text{eV}$ (see Methods) cannot be resolved experimentally, the Zeeman splitting at 8 T ($gu_B B = 0.93$ meV assuming $g = 2$; u_B is Bohr magneton) would greatly exceed the superconducting gap (~ 0.27 meV). This suggests the observed ZBPs in UTe_2 likely correspond to a true zero mode, and thus not CdGM states. Spatially, as shown in the $g(\mathbf{r}, V)$ (Fig. 3c) and corresponding d^2g/dV^2 (Fig. 3d) spectra taken at $B = 4$ T across a vortex along the \mathbf{a} -axis direction, such ZBP extends over 6 nm from the VC without displaying an X-shaped splitting typically observed from CdGM states^{20,21} (real space images and more linecuts are shown in Extended Data Fig. 6).

To provide insight on the origin of the robust ZBPs, we consider the two scenarios (1) and (2) separately, where the OP under field is non-chiral and chiral, respectively. In scenario (1), a non-chiral p -wave Cooper-pair condensate (with a single- or multi-component OP) is expected to host Majorana Kramers pairs on the boundaries under zero magnetic field⁴⁶. In the presence of a magnetic field, one would naively expect that no MZM pair can survive in a magnetic VC since the TRSB Zeeman splitting would hybridize the pair and push them each to finite energies. However, as a crystalline superconductor, UTe_2 possesses a mirror plane (Fig. 1a) perpendicular to the \mathbf{a} -axis, containing the vortex lines. In fact, crystalline symmetries have been previously proposed to provide topological protection for vortex MZMs in various non-chiral topological superfluid/superconductors^{13,21,47}. Here, we theoretically show that integer numbers of MZMs can coexist in a full quantum vortex, where the vortex line can be viewed as an individual 1D system containing additional topological protection from the mirror symmetry.

In the absence of a magnetic field, the superconducting state is described by a mean-field Bogoliubov de Gennes (BdG) Hamiltonian $H_{\text{BdG}} = \sum_{\mathbf{r}, \mathbf{r}'} \psi_{\mathbf{r}'}^\dagger \begin{pmatrix} H_0 & \Delta \\ \Delta^\dagger & -H_0 \end{pmatrix} \psi_{\mathbf{r}}$ where $\psi_{\mathbf{r}} = (c_{\mathbf{r}\uparrow}, c_{\mathbf{r}\downarrow}, c_{\mathbf{r}\uparrow}^\dagger, c_{\mathbf{r}\downarrow}^\dagger)^T$ is the Nambu spinor, $c_{\mathbf{r}s}^\dagger$ creates an electron at position \mathbf{r} with spin s , H_0 is a spin-degenerate normal state, and Δ is the non-chiral spin-triplet OP. The superconducting Hamiltonian H_{BdG} belongs to the topological class DIII¹⁵, which preserves the TRS $\Theta = i\sigma_y \otimes \tau_0 \kappa, \mathbf{r} \rightarrow \mathbf{r}$, the particle-hole anti-symmetry $P = \sigma_0 \otimes \tau_x \kappa, \mathbf{r} \rightarrow \mathbf{r}$, and an in-plane mirror reflection $M_x = i\sigma_x \otimes \tau_z, (x, y, z) \rightarrow (-x, y, z)$, where σ_i and τ_i are Pauli matrices in the spin and Nambu bases and κ is the complex conjugate operation. Here, we have renamed \mathbf{a} -axis into x and assumed that the OP Δ is even under reflection M_x . When a magnetic field $\mathbf{B} = B\hat{z}$ is applied, the 1D vortex lines experience a Zeeman splitting $H_z \propto \sigma_z \otimes \tau_z$. As a result, the full Hamiltonian $H'_{\text{BdG}} = H_{\text{BdG}} + H_z$ loses the time-reversal and reflection symmetries since $[\Theta, H_z] \neq 0$ and $[M_x, H_z] \neq 0$. Nonetheless, these vortex lines remain invariant under an effective TRS $\Theta' = M_x \Theta = -i\sigma_z \otimes \tau_z \kappa$ as well as the particle-hole anti-symmetry P since $[\Theta', H'_{\text{BdG}}] = 0$ and $\{P, H'_{\text{BdG}}\} = 0$. Note that this effective TRS Θ' is fundamentally different from the original Θ in that instead of $\Theta^2 = -1$, the new symmetry has $(\Theta')^2 = 1$ due to the embedded reflection M_x . Therefore, unlike Θ , Θ' no longer dictates the existence of Majorana Kramers pairs, which is a well-established quantum mechanical consequence⁴⁸. Instead, a vortex line as an independent 1D system belongs to a symmetry-protected topological system in class BDI, which allows any integer numbers of MZMs at the two ends of the vortex line¹⁵, including the case of a single MZM. Although spatially non-splitting ZBPs can also result trivially from anisotropic superconductors⁴⁹, considering the persistence of the ZBPs at 8 T and theoretical considerations here together, the observed ZBPs in UTe₂ are not inconsistent with MZMs from the topological vortex lines protected by mirror, time-reversal, and particle-hole symmetries in a non-chiral p -wave superconductor.

In scenario (2) where a chiral multi-component OP is favored under a magnetic field, the superconducting mean-field Hamiltonian under a magnetic field H'_{BdG} can break the effective TRS Θ' . This is because in contrast to scenario (1), the Θ -breaking pairing term does not have to preserve Θ' . In the case where Θ' is broken by the pairing term, the only surviving symmetry in the vortex lines is the particle-hole symmetry P . These vortex lines are thus 1D systems in topological class D, which are topologically equivalent to Kitaev chains and are well expected to host single MZM at the two ends of a vortex line⁵⁰, leading to ZBPs surviving up to high magnetic fields.

To first order, the spatial visualization of ZBPs further enables extraction of orientation-dependent superconducting coherence lengths $\xi(\theta)$. The zero-bias conductance image of a single vortex measured at low field (0.5 T) is shown in Fig. 3e after two-fold symmetrization [$g_S(\mathbf{r}, 0\text{ V})$] to suppress spatially varying $g(\mathbf{r}, 0\text{ V})$ background under zero-field (Extended Data Fig. 2). $g_S(\mathbf{r}, 0\text{ V})$ is then fitted with an exponential decay $g_S(\mathbf{r}, 0\text{ V}) = De^{-ir/\xi} + F$ for each angle θ , where D and F are constants (see Methods), and the extracted $\xi(\theta)$ is shown in Fig. 3f. Figure 3g shows the results for directions along and perpendicular to the \mathbf{a} -axis of UTe_2 , revealing a strong anisotropy with $\xi_a \approx 12\text{ nm}$ and $\xi_{b^*} \approx 4\text{ nm}$. The larger coherence length along the \mathbf{a} -axis direction contrasts with bulk measurements that determined the upper critical field to be smallest along the \mathbf{a} axis (i.e., ξ_a is expected to be the smallest)^{3,8}. Furthermore, if we calculate the upper critical field along $\hat{\mathbf{n}}_{011}$, we have $H_{c2}^{011} = \frac{\Phi_0}{2\pi\xi_a\xi_{b^*}} = 6.9\text{ T}$, which is significantly smaller than that ($\sim 20\text{ T}$) determined from bulk measurements¹¹. Such apparent paradoxes could be reconciled if there is more than one superconducting condensate (e.g., existence of multi-band or surface superconductivity), where the one with weaker pairing and a larger coherence length contributes to STM vortex imaging as in the case of MgB_2 ⁵¹. The weakened surface superconductivity could also be consistent with a competing surface-only charge density wave detected previously^{7,52,53}. Moreover, as the magnetic field is increased, the size of vortices decreases following roughly a $1/\sqrt{B}$ trend while preserving a large anisotropy (Extended Data Fig. 7). If UTe_2 were a weak-coupling BCS superconductor, this would be consistent with predictions at high fields⁵⁴. Considering the discussions above and similar field-induced vortex-shrinking observed in $\text{Cu}_x\text{Bi}_2\text{Se}_3$ ⁵⁵, this observation could again be consistent with the presence of distinct and weakened surface superconductivity in UTe_2 .

Mirror-asymmetric vortex doublets

In addition to the high anisotropy, close examination of vortex images reveals that while the mirror symmetry is preserved along the \mathbf{a} -axis, the mirror symmetry along the \mathbf{b}^* -axis is broken. This is most clearly seen in Figs. 4a,b. The locations of vortices (black ellipse) can be identified in $g(\mathbf{r}, 0\text{ V})$ in Fig. 4a under $B = 4\text{ T}$. Simultaneously acquired $dg/dV(\mathbf{r}, 267\text{ }\mu\text{V})$ image in Fig. 4b clearly shows a doublet structure for each vortex indicated by pairs of blue-pink ellipses. Phenomenologically, such a doublet structure undergoes a transition at $|B| \sim 2.5\text{ T}$ (i.e., blue-pink vs pink-blue; Extended Data Figs. 8, 9) as quantitatively depicted in Fig. 4c. Here, we have plotted the mirror-asymmetry index $\frac{L}{d} - 0.5$ as a function of B , where the length L is schematically defined in Fig. 4b. Applying a small in-plane magnetic field in different directions does not alter such doublet structures within measurement precision (Extended Data Fig. 10), suggesting the asymmetry cannot originate from small misalignment between the magnetic field direction and the $\hat{\mathbf{n}}_{011}$ direction of UTe_2 . While dg/dV imaging provides the first signature of exotic vortex

structures, we explore this further by extracting the apparent superconducting gap $\Delta^*(\mathbf{r})$ in Fig. 4d (see Methods) via spectroscopic imaging over multiple vortices. The VCs have nearly zero gap magnitudes with one indicated by a black ellipse. Unprecedented in known superconductors (to our knowledge), although Δ^* recovers to around the zero-field gap of $270 \mu\text{eV}$ while moving away from the VC in the $+\mathbf{b}^*$ direction, Δ^* increases up to $400 \mu\text{eV}$ in the $-\mathbf{b}^*$ direction and forms a crescent domain of similar size to the VC with a mutual separation of $W = 5\sim 10 \text{ nm}$ (Fig. 4d and Extended Data Fig. 8). Such crescent-shaped structure is also manifested in $dg/dV(\mathbf{r}, -333 \mu\text{V})$ in Fig. 4e. To visualize such enhanced apparent gap, differential conductance spectra taken at various locations around a VC (red crosses in Fig. 4d) as well as under zero magnetic field are compared in Fig. 4f, where an enlarged gap with a similarly shaped spectrum is seen in the crescent domain (left of VC). Figures 4g,h display a series of $g(\mathbf{r}, V)$ and $d^2g/dV^2(\mathbf{r}, V)$ spectra taken along a line parallel to the \mathbf{b}^* -axis as indicated in Fig. 4a. Clearly, the recovery of Δ^* on the two sides of a vortex is highly asymmetric, with an overshooting Δ^* on the left side of each vortex, regardless of field strength and direction (Extended Data Figs. 6, 8, 11,12).

Possible origins of asymmetric vortex structures

The field-dependence of the mirror-asymmetry of vortex structures can shed light on the possible origin of it. As shown in Fig. 4c and Extended Data Figs. 8,9,11, the apparent asymmetry in both $\frac{dg}{dV}$ imaging (represented by $\frac{L}{d} - 0.5$) and the apparent gap Δ^* remains unchanged (i.e., no flipping) under the switching of magnetic field directions. If magnetic vortex lines were to extend through the UTe_2 crystal along $\hat{\mathbf{n}}_{011}$ with preserved mirror-asymmetry, we would expect the asymmetry to be opposite if the direction of B is flipped, contradicting experiments (Extended Data Fig. 13). This suggests instead mechanisms that lock the vortex asymmetry to the lattice asymmetry on the (011) surface. We first consider trivial possibilities. For example, the vortex asymmetry could result from tilted vortex lines considering the strong magnetic anisotropy² of UTe_2 (Extended Data Fig. 13). However, significant changes of Δ^* up to $100 \mu\text{eV}$ (Extended Data Fig. 12) are unlikely in this scenario. Naively, another possibility is a mirror-asymmetric surface Doppler effect^{56,57} from a B-field induced anomalous supercurrent flowing on the surface with a velocity \mathbf{v}_a around the \mathbf{b}^* -axis (Extended Data Fig. 14). This will result in different net superfluid velocities v_s on the two sides of a vortex and therefore different coherence peak splitting that is twice of the Galilean energy boost $\delta E_{\mathbf{k}_F} = \hbar \mathbf{k}_F \cdot \mathbf{v}_s$ (Methods), where \mathbf{k}_F is the Fermi wavevector. Indeed, such considerations are generally true and by assuming an isotropic superconducting gap and circular Fermi surface, one can obtain $v_a \approx 12.6 \text{ m/s}$ (Methods, Extended Data Fig. 14). However, in the unique case of anisotropic UTe_2 where the maximum superconducting gap lies along the \mathbf{b}^* -axis (Fig. 3f) — perpendicular to the hypothetical anomalous flow along the \mathbf{a} -axis— we have $\delta E_{\mathbf{k}_F} = 0$ for $\mathbf{k}_F = \pm k_F \hat{\mathbf{b}}^*$. This suggests no splitting of the coherence peak, which

reflects the largest gap at $\mathbf{k}_F = \pm k_F \hat{\mathbf{b}}^*$, and thus no change of the apparent gap Δ^* (Extended Data Fig. 14). Therefore, the vortex asymmetry is unlikely a consequence of the Doppler effect from an anomalous surface supercurrent. It is also unlikely that a weaker surface superconductivity postulated above is responsible for the observed asymmetric vortices with an enhanced Δ^* and sharper coherence peaks on one side of the VC compared to zero-field measurements (Fig. 4f and Extended Data Figs. 6, 8, 11, 12). Another candidate is the double-core vortices in non-chiral p -wave superfluid $^3\text{He-B}$ under low temperature and pressure^{27,58}. The double-core vortices are each composed of two half-quantum vortices (HQVs) that bound to each other. While HQVs are recently predicted⁵⁹ to exist in UTe_2 if assuming a chiral p -wave OP, the crescent domain has an enhanced gap Δ^* as opposed to a suppressed OP, precluding the possibility of the observed doublets being double-core vortices. Recent measurements using superconducting quantum interference devices on UTe_2 also detected no signatures of HQVs⁶⁰.

We now discuss our conjectures for the origins of the observed vortex doublet. As mentioned earlier, the applied magnetic field along $\hat{\mathbf{n}}_{011}$ is expected to induce a multi-component OP, which has been known for hosting complex and mirror-asymmetric vortex structures in various multi-component superfluid and superconductors^{33,61,62}. This is because regardless of whether the multi-component OP breaks TRS, a subdominant OP can be induced near the VCs of a dominant OP. While the dominant components are generally expected to form vortices with symmetric shapes, depending on the crystalline symmetry group, the induced OP can energetically favor an axis-asymmetric real-space pattern, leading to an asymmetric superconducting regime nearby. In fact, mirror-asymmetric vortex structures of this kind (e.g., triangular or crescent^{33,61}) have been predicted in topological superfluid ^3He (ref. 61) and unconventional superconductors with different crystalline symmetries, including UPt_3 (ref. 33) and cuprates with an induced s -wave component around a d -wave core⁶². The observed UTe_2 vortex doublet thus resembles a vortex structure of this kind. Furthermore, the same conjecture of a field-induced multi-component OP, which likely contains the fully gapped irrep A_u due to energetics, can possibly account for field-induced sharper coherence peaks (Fig. 4f, Extended Data Fig. 6).

Conclusions

In ultra-pure UTe_2 , we uncover anisotropic, time-reversal invariant superconductivity at zero magnetic field, along with persistent VC ZBPs up to 8 T, signatures of surface superconductivity, and mirror-asymmetric vortex doublets—each comprising domains with suppressed and enhanced superconducting gaps. Theoretical analysis suggests the robust ZBP to be consistent with symmetry-protected MZMs. We propose that a field-induced multi-component OP, arising from the reduced point group symmetry, can potentially lead to the emergence of mirror-asymmetric vortices by condensing a subdominant OP. The interplay of anisotropic

superconductivity, spin-triplet pairing, spin-orbit coupling, and \mathbf{d} vector rotations under a magnetic field implies rich physics to be explored but also challenges for theoretical modeling. The exact forms of OPs and their vortex solutions under magnetic fields deserve future exploration.

Methods

Crystal growth and transport measurements

Single crystals of UTe_2 were grown through a molten salt technique using an equimolar mixture of sodium chloride (NaCl) and potassium chloride (KCl) as reported previously (ref. 12). The crystallographic structure of our crystals was verified at room temperature by a Bruker D8 Venture single-crystal x-ray diffractometer equipped with Mo K- α radiation. To ensure that the samples only show a single superconducting transition temperature, specific heat measurements were performed using a Quantum Design calorimeter that utilizes a quasi-adiabatic thermal relaxation technique. Electrical resistivity was measured with an alternating current resistance bridge using a standard four-point technique with current along the [100] direction. The RRR is extracted by fitting the temperature-dependent resistivity $\rho(T)$ with $\rho = AT^2 + \rho_0$ in the low-temperature region before the superconducting transition (Extended Data Fig. 1). Then RRR is calculated by $\text{RRR} = \rho(300 \text{ K})/\rho_0$.

Scanning tunneling microscopy and spectroscopy

STM experiments are performed on a Unisoku USM1300J systems at a base temperature of 0.3 K. The UTe_2 crystals are cleaved at a temperature of ~ 10 K under ultrahigh vacuum ($\sim 1 \times 10^{-10}$ Torr) before loaded into the STM head. Both mechanically cut Nb and PtIr tips are used for measurements after thorough outgassing via heating in vacuum. The zero-field differential conductance spectrum shown in Fig. 4f and the map shown in Extended Data Fig. 2 are measured with PtIr tips, while all other data are acquired using Nb tips. While the Nb tips are superconductive under zero magnetic field and allow us to extract the UTe_2 gap via multiple Andreev reflections (Extended Data Fig. 2), the Nb tips become normal and metallic under all magnetic fields (> 0.3 T) reported in this study such that no deconvolution of spectra is necessary. Field-cooling is performed by applying a magnetic field at a temperature above T_c followed by cooling down to the base temperature of 0.3 K. STM data are acquired using SPECS Nanonis electronics. Spectroscopic measurements ($I - V$, $g - V$, and dg/dV) are performed using a built-in lock-in amplifier in Nanonis with a modulation of $100 \mu\text{V}$, while dg/dV spectra can also be acquired via numerical derivative of $g - V$ spectra. d^2g/dV^2 spectra are all obtained via numerical derivative of $g - V$ spectra. A typical lock-in modulation frequency is 983.7 Hz. MATLAB and Gwyddion software are used for data processing.

Coherence length extraction

The $g(\mathbf{r}, 0 \text{ V})$ images are first smoothed by a Gaussian filter of 0.5 pixel to reduce random noise, and then symmetrized in a twofold fashion along the \mathbf{a} and \mathbf{b}^* directions to generate $g_S(\mathbf{r}, 0 \text{ V})$. Strictly speaking, because of the mirror-asymmetric vortices, symmetrization along the

\mathbf{b}^* direction is not justified. However, to first order, this approach helps suppress spatially varying in-gap DOS existing at zero field, providing a good estimate of the coherence lengths. Then, for each vortex, the $g_S(\mathbf{r}, 0 V)$ image is fitted with a function $g_S(\mathbf{r}, 0 V) = D e^{-r/\xi} + F$ along different directions, where the origin of \mathbf{r} is defined to be the center of each VC. The constant F represents and is determined by the zero-energy DOS far from each vortex, and the constant D is a scaling factor.

Superconducting gap extraction

To precisely extract the apparent superconducting gaps Δ^* , defined as half of the voltage separation between two coherence peaks in differential conductance spectra, we use a curvature-based analysis method⁶³ that have shown effectiveness in peak extractions in STM⁶⁴. Each point spectrum $g(V)$ is first interpolated using a cubic spline fit. Then, a local curvature of each spectrum is calculated as

$$C(V) = -\frac{d^2g/V^2}{[C_0+(dg/dV)^2]^{3/2}} \quad (2)$$

where C_0 is a constant. In this way, the peak positions of g can be extracted accurately from the local maxima of C . ZBPs detected within a voltage range of $-150 \mu V$ to $150 \mu V$ indicate the location of VCs. The validity of detected peaks is verified manually. Once the ZBP locations are determined, the gap is set to zero at those locations. To extract Δ^* , locations of coherence peaks are detected in the energy ranges of $(-450 \mu V, -200 \mu V)$ and $(200 \mu V$ to $450 \mu V)$. The extracted gap maps are manually verified.

Estimation of energy separation of CdGM states

Discrete CdGM states^{19,65} have energy separations of $\delta E_n = \frac{|\Delta|^2}{E_F}$. Because $E_F = \frac{\hbar k_F v_F}{2}$ and $\xi = \frac{\hbar v_F}{\pi |\Delta|}$, we have $\frac{|\Delta|}{E_F} = \frac{2}{\xi \pi k_F}$ and thus $\delta E_n = \frac{2|\Delta|}{\xi \pi k_F}$. For UTe₂, we can take $k_F \sim 3/\text{nm}$ (ref. 66), $|\Delta| = 0.27 \text{ meV}$, and $\xi = 4 \text{ nm}$, and obtain $\frac{|\Delta|}{E_F} \approx 0.05$. Since $\frac{T}{T_c} = 0.14$ for $T = 0.3 \text{ K}$, the quantum limit situation ($\frac{T}{T_c} \ll \frac{\Delta}{E_F}$) is not satisfied⁶⁵ and $\delta E_n = \frac{|\Delta|^2}{E_F} \approx 14 \mu\text{eV}$ is beyond the energy resolution at 0.3 K, where $k_B T = 26 \mu\text{eV}$.

DOS simulation considering the Doppler effect

The calculation and extraction of superfluid flow velocity by measuring quasiparticle DOS is detailed in Ref. 56. Briefly, assuming a circular Fermi surface, a Galilean energy boost $\delta E_{\mathbf{k}} \equiv \hbar \mathbf{k} \cdot \mathbf{v}_s(\mathbf{r})$ will alter the spectrum of a quasiparticle $|\mathbf{k}\rangle$ in a flowing superfluid: $E_{\mathbf{k}} = \pm \sqrt{\varepsilon_{\mathbf{k}}^2 + |\Delta|^2} + \hbar \mathbf{k} \cdot \mathbf{v}_s$, where $\varepsilon_{\mathbf{k}}$ is the normal-state band structure and \mathbf{v}_s is the superfluid velocity. Using the Dynes formula, the quasiparticle DOS with a finite superfluid flow can be written as

$$N(E) = \text{sign}(E) \int_0^{2\pi} \text{Re} \left(\frac{E - \delta E_{\mathbf{k}_F} - i\gamma}{\sqrt{(E - \delta E_{\mathbf{k}_F} - i\gamma)^2 - |\Delta(\theta)|^2}} \right) d\theta \quad (3)$$

The consequence of a finite $\delta E_{\mathbf{k}_F}$ for \mathbf{k}_F along the direction of the largest superconducting gap is that the superconducting coherence peak exhibits a symmetric splitting of $2|\delta E_{\mathbf{k}_F}|$, leading to a decreased Δ^* by $|\delta E_{\mathbf{k}_F}|$ and reduced coherence peak heights as observed previously^{56,57} and shown in Extended Fig. 14.

Acknowledgements

The authors thank M. Eskildsen, J. Sauls, and N. Glusceвич for valuable discussions. N.S., M.T., J.M., F.C. and X.L. acknowledge support from the U.S. Department of Energy (DOE), Office of Science, Office of Basic Energy Sciences under Award Numbers DE-SC0025021 (2nd derivative vortex imaging) and DE-SC0024291 (general STM operation), and the Stavropoulos Center for Complex Quantum Matter at the University of Notre Dame. Y.-T.H. acknowledges support from National Science Foundation Grant No. DMR-2238748. N.S. and M.T. acknowledge support from the Notre Dame Materials Science and Engineering Fellowship. Work at Los Alamos was supported by the U.S. Department of Energy, Office of Science, National Quantum Information Science Research Centers. M.M.B. acknowledges support from the Los Alamos Laboratory Directed Research and Development program.

Author contributions

X.L. conceived the project. N.S., M.T., and J.M. performed the measurements. M.M. B, S.M.T., and P.F.S.R. synthesized the crystals and performed electrical resistivity measurements. Y.-T.H. performed theoretical analysis. N.S., M. T., J.M. and F.C. performed data analysis. X.L. and Y.-T.H. wrote the manuscript with input from all authors. All authors contributed to data interpretation.

Data availability

All data needed to evaluate the conclusions in the paper are present in the paper and/or the Extended Data. Additional data related to this paper may be requested from the authors.

Competing financial interests

The authors declare no competing financial interests.

Figures

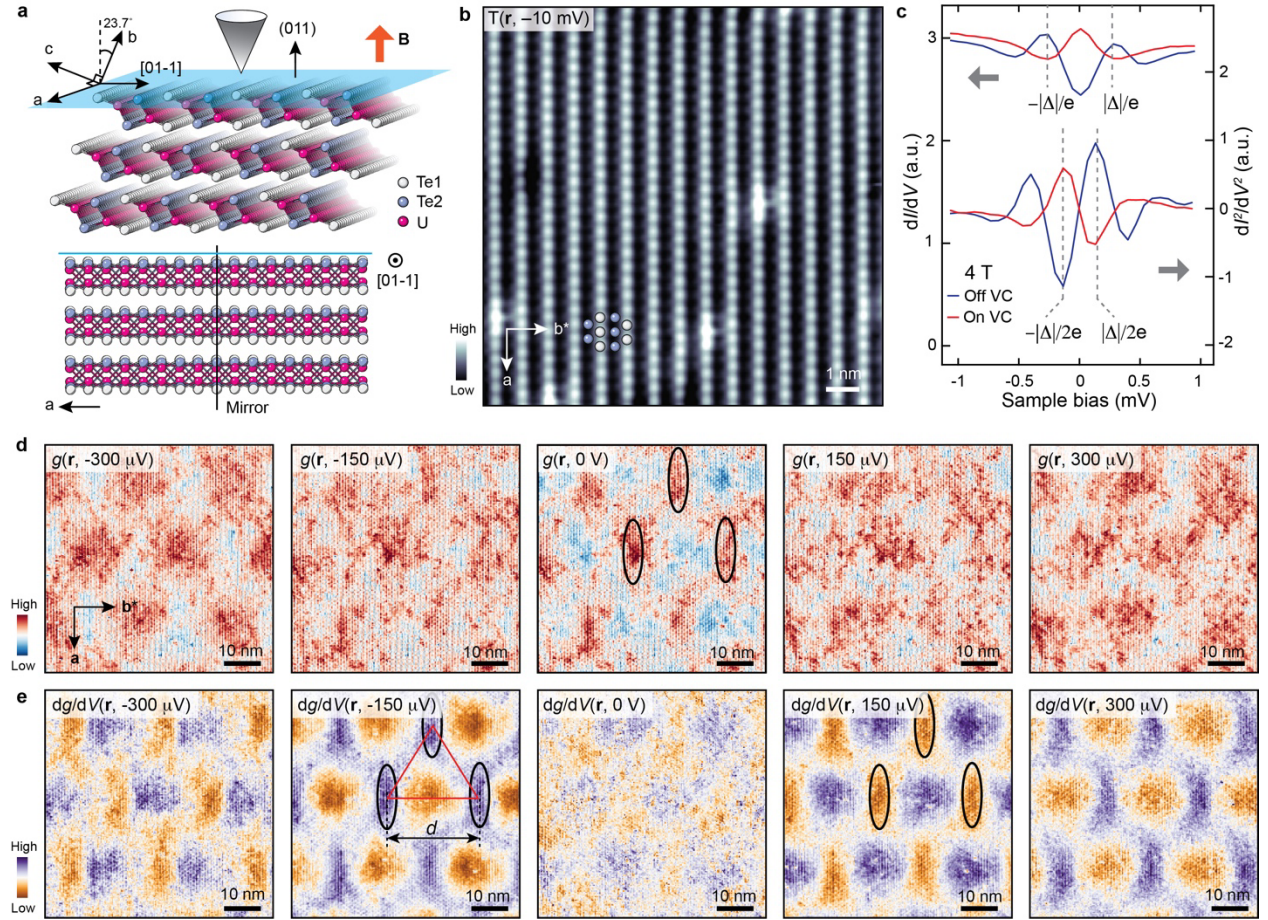


Figure 1. Visualizing superconducting vortices of UTe_2 .

a, Top: schematic of measurement setup. STM images the (011) surface of UTe_2 with the magnetic field applied in the normal direction of (011) surface (defined as \hat{n}_{011} direction), which is 23.7° rotated from the crystallographic b axis in the b - c plane. Bottom: a side view of the UTe_2 crystal with the magnetic field direction pointing vertically up. A mirror plane containing the vortex lines is indicated. **b**, A typical topographic image of UTe_2 (011) surface with overlaid Te1 and Te2 atoms (setpoint: $V_S = -10$ mV, $I_0 = 1$ nA). **c**, Differential conductance (g) and dg/dV spectra taken on and off VCs of UTe_2 under $B = 4$ T. Maximal contrast of vortices are expected at energies around $\pm|\Delta|/2e$. **d**, $g(r, V)$ and **e**, $dg/dV(r, V)$ images acquired at $B = 4$ T. The triangular lattice of vortices are indicated by black ellipses with inter-vortex distance d . The vortices are best visualized in $dg/dV(r, V \approx \pm|\Delta|/2e \approx \pm 150$ μ V).

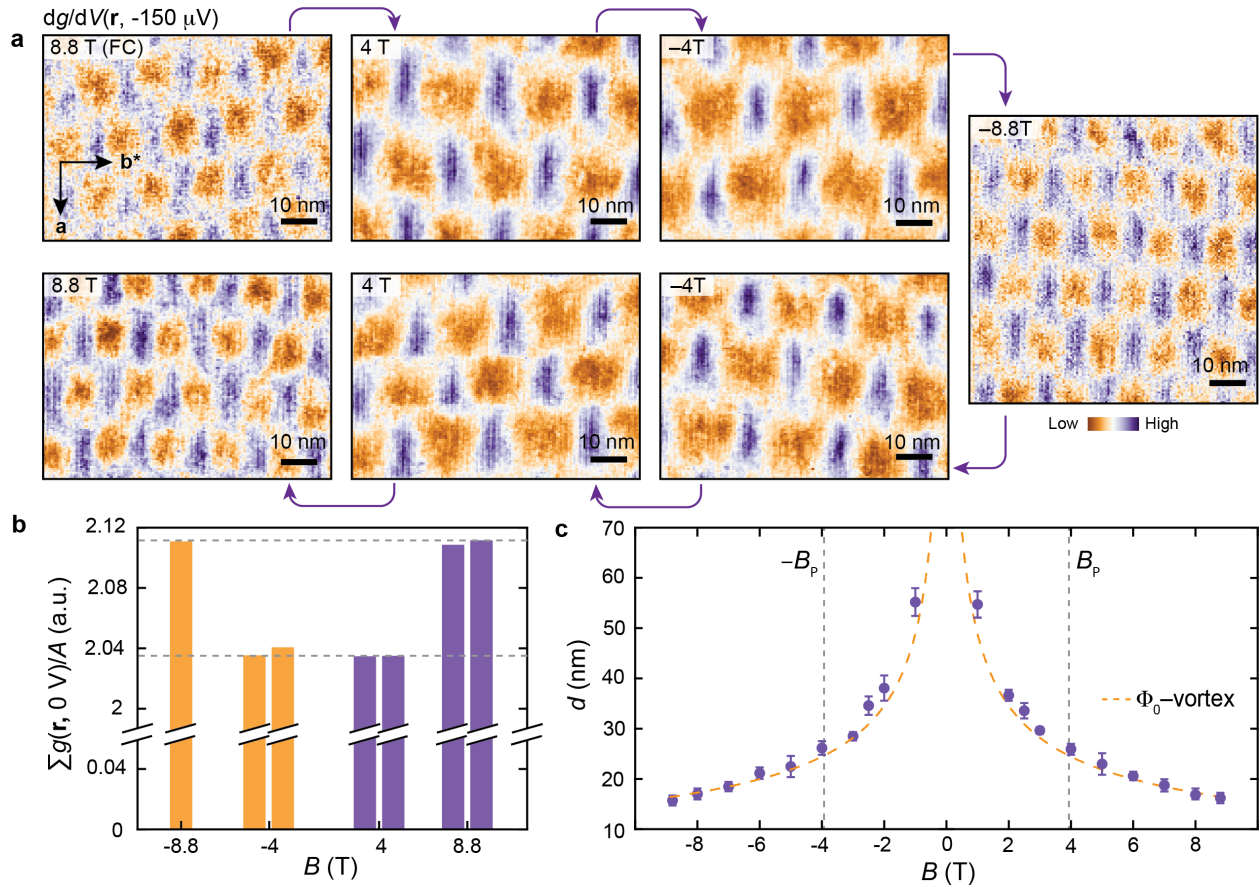


Figure 2. Time-reversal invariant superconductivity

a, A series of $dg/dV(\mathbf{r}, -150 \mu\text{V})$ images of vortices at different fields under a single field-cooling (FC) with $B = 8.8$ T. No discernable differences of the vortex structure can be observed. The slight tilts of the VLs are likely due to slow vortex creeping. **b**, Areal integrated zero-energy DOS at different fields, showing differences $< 0.3\%$ between different field polarities. **c**, Extracted inter-vortex distance as a function of B , showing agreement with single-flux-quantum (Φ_0) vortices. The vertical lines indicate the Pauli paramagnetic limit $B_p \approx 3.9$ T.

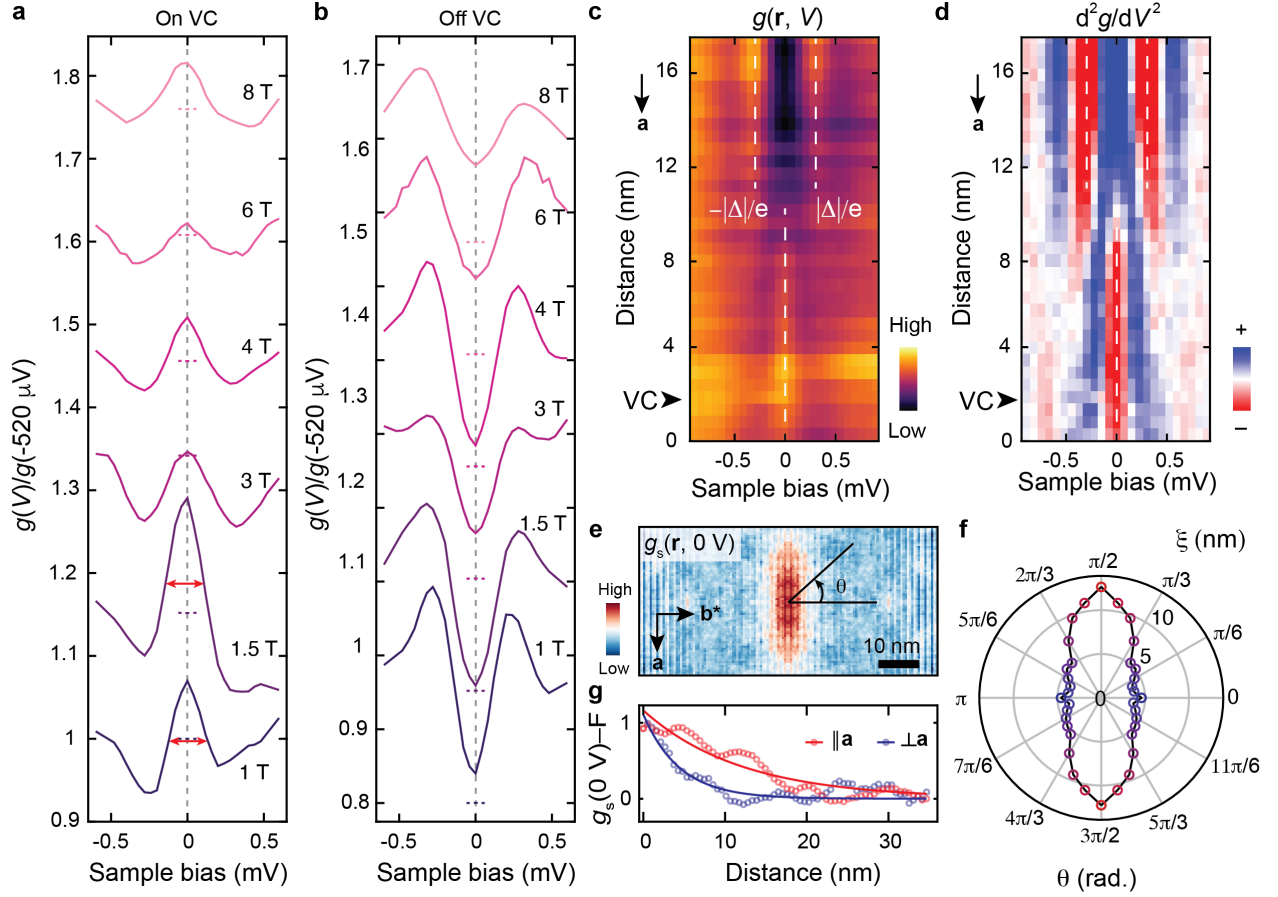


Figure 3. Persistent zero-bias peak and coherence lengths extraction

a, Normalized differential conductance spectra $g(V)/g(-520 \mu\text{V})$ measured at the VCs under different magnetic fields showing prominent ZBPs. The dashed lines indicate a level of $g(V)/g(-520 \mu\text{V}) = 1$ for each spectrum. The red double arrows correspond to $250 \mu\text{V}$, indicating the FWHMs of ZBPs at low fields. **b**, Normalized differential conductance spectra $g(V)/g(-520 \mu\text{V})$ measured far from vortices under different magnetic fields showing almost unaffected superconductivity gap size and gap filling at higher fields. The dashed lines indicate a level of $g(V)/g(-520 \mu\text{V}) = 0.8$ for each spectrum. **c**, A series of $g(V)$ and **d**, d^2g/dV^2 spectra taken across a vortex at $B = 4 \text{ T}$ along the **a**-axis direction (indicated by an arrow) showing a non-splitting ZBP extending over 6 nm in one direction from the core (indicated by an arrow head). **e**, Symmetrized zero-bias conductance image $g_s(\mathbf{r}, 0 \text{ V})$ at $B = 0.5 \text{ T}$ of a single vortex. The angle θ is defined with respect to the \mathbf{b}^* direction. **f**, Extracted angle-dependent coherence length. **g**, $g_s(\mathbf{r}, 0 \text{ V})$ and fittings for directions along and perpendicular to the **a**-axis of UTe_2 , revealing anisotropic superconductivity with $\xi_a \approx 12 \text{ nm}$ and $\xi_{b^*} \approx 4 \text{ nm}$.

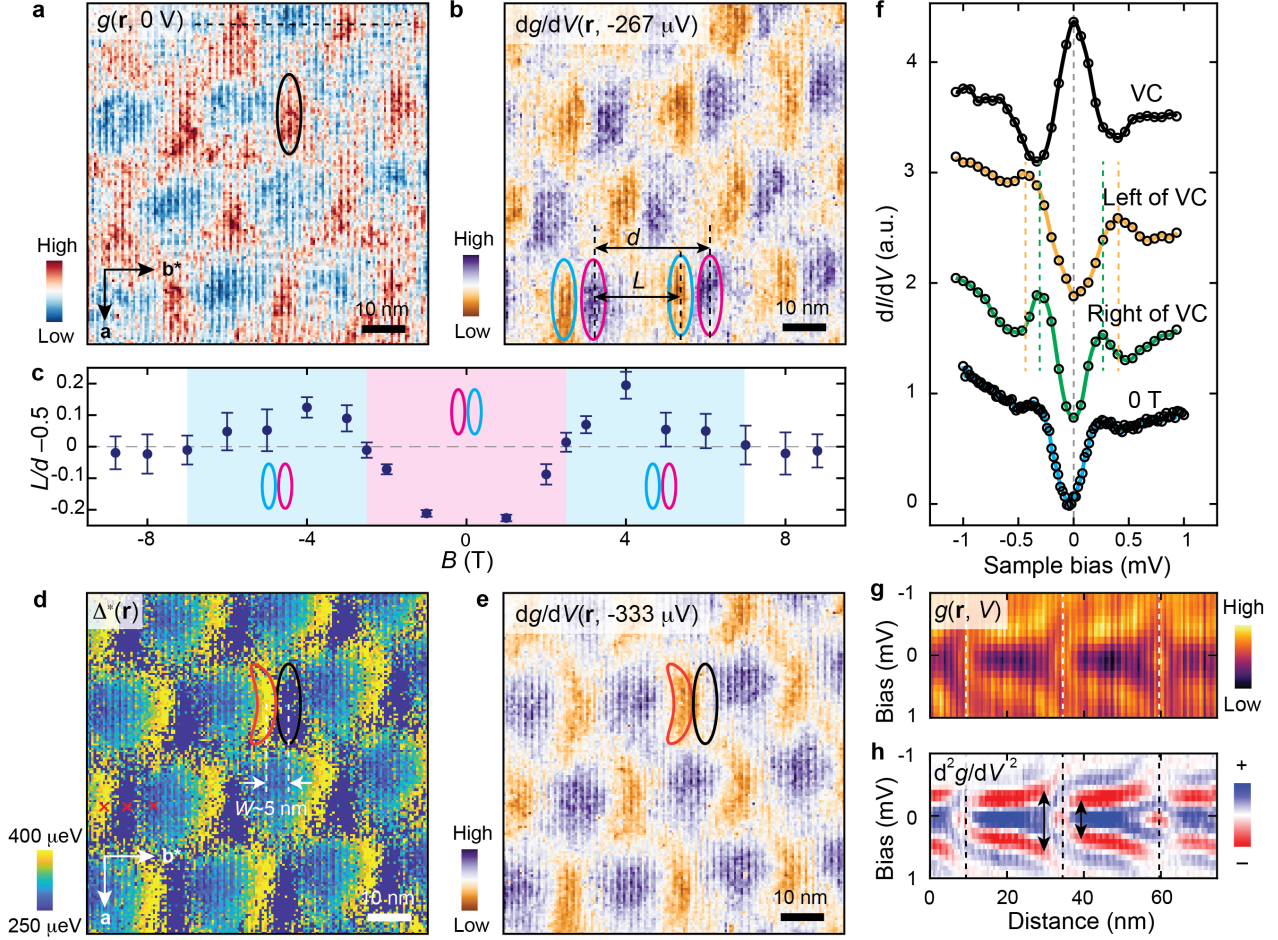


Figure 4. Mirror-asymmetric vortex doublet

a, Zero-bias conductance image of vortices under $B = 4$ T. The black ellipse indicates the location of a VC. **b**, Simultaneously acquired $dg/dV(\mathbf{r}, -267 \mu\text{V})$ image showing each vortex forming a doublet structure as indicated by the blue-pink pairs. Note that the pink ellipses do not necessarily correspond to the locations of VCs (black ellipse). **c**, A transition of the doublet structures as indicated by the blue-pink and pink-blue ellipses is observed symmetrically as a function of magnetic field. This is quantitatively demonstrated using an index defined as $\frac{L}{d} - 0.5$. **d**, Extracted apparent superconducting gap $\Delta^*(\mathbf{r})$ showing a domain of enhanced gap (red crescent) on the left side of each VC (black ellipse), which can also be observed in **e**, simultaneously acquired $dg/dV(\mathbf{r}, -333 \mu\text{V})$. The separation between the ellipse and the VC is around ξ_b^* . **f**, $g(V)$ spectra at locations indicated by the red crosses in (d) and at zero magnetic field, demonstrating an enhanced gap up to $\sim 400 \mu\text{eV}$ in the crescent domain. **g**, A series of $g(V)$ and **h**, d^2g/dV^2 spectra taken along the dashed line in (a) showing enhanced gaps on the left side of each VC as indicated by the double arrows.

References

- 1 Blatter, G., Feigelman, M.V., Geshkenbein, V.B., Larkin, A.I. & Vinokur, V.M. Vortices in high-temperature superconductors. *Rev. Mod. Phys.* **66**, 1125 (1994).
- 2 Aoki, D. et al. Unconventional superconductivity in UTe₂. *J. Phys.: Condens. Matter* **34**, 243002 (2022).
- 3 Ran, S. et al. Nearly ferromagnetic spin-triplet superconductivity. *Science* **365**, 684–687 (2019).
- 4 Hayes, I. et al. Multicomponent superconducting order parameter in UTe₂. *Science* **373**, 797–801 (2021).
- 5 Jiao, L. et al. Chiral superconductivity in heavy-fermion metal UTe₂. *Nature* **579**, 523–527 (2020).
- 6 Duan, C. et al. Resonance from antiferromagnetic spin fluctuations for superconductivity in UTe₂. *Nature* **600**, 636–640 (2021).
- 7 Gu, Q. et al. Detection of a pair density wave state in UTe₂. *Nature* **618**, 921–927 (2023).
- 8 Ran, S. et al. Extreme magnetic field-boosted superconductivity. *Nat. Phys.* **15**, 1250-1254 (2019).
- 9 Azari, N., et al. Absence of Spontaneous Magnetic Fields due to Time-Reversal Symmetry Breaking in Bulk Superconducting UTe₂. *Phys. Rev. Lett.* **131**, 226504 (2023).
- 10 Ajeesh, M.O., et al. Fate of time-reversal symmetry breaking in UTe₂. *Phys. Rev. X* **13**, 041019 (2023).
- 11 Wu, Z., Weinberger, T.I., Chen, J. & Eaton, A.G. Enhanced triplet superconductivity in next-generation ultraclean UTe₂. *Proc. Natl. Acad. Sci. U. S. A* **121**, e2403067121 (2024).
- 12 Sakai, H. et al. Single crystal growth of superconducting UTe₂ by molten salt flux method. *Phys. Rev. Materials* **6**, 073401 (2022).
- 13 Fang, C., Gilbert, M. J. & Bernevig, B. A. New class of topological superconductors protected by magnetic group symmetries. *Phys. Rev. Lett.* **112**, 106401 (2014).
- 14 Sata, M. & Ando, Y. Topological superconductors: a review. *Rep. Prog. Phys.* **80**, 076501 (2017).
- 15 Schnyder, A.P., Ryu, S., Furusaki, A. & Ludwig, A.W.W. Classification of topological insulators and superconductors in three spatial dimensions. *Phys. Rev. B* **78**, 195125 (2008).
- 16 Beenakker, C.W.J. Search for Majorana Fermions in Superconductors. *Annu. Rev. Condens. Matter Phys.* **4**, 113–36 (2013).
- 17 Lutchyn, R.M. et al. Majorana zero modes in superconductor-semiconductor heterostructures. *Nat. Rev. Mater.* **3**, 52-68 (2018).
- 18 Zhang, P. et al. Observation of topological superconductivity on the surface of an iron-based superconductor. *Science* **360**, 182-186 (2018).
- 19 Wang, D. et al. Evidence for Majorana bound states in an iron-based superconductor. *Science* **362**, 333-335 (2018).
- 20 Xu, J.-P. et al. Experimental detection of a Majorana mode in the core of a magnetic vortex inside a topological insulator-superconductor Bi₂Te₃/NbSe₂ heterostructure. *Phys. Rev. Lett.* **114**, 017001 (2015).
- 21 Liu, T. et al. Signatures of hybridization of multiple Majorana zero modes in a vortex. *Nature* **633**, 71-76 (2024).
- 22 Nadj-Perge, S. et al. Observation of Majorana fermions in ferromagnetic atomic chains on a superconductor. *Science* **346**, 602-607 (2014).

-
- 23 Feldman, B. E. et al. High-resolution studies of the Majorana atomic chain platform. *Nat. Phys.* **13**, 286–291 (2017).
- 24 Kezilebieke, S. et al. Topological superconductivity in a van der Waals heterostructure. *Nature* **588**, 424-428 (2020).
- 25 Palacio-Morales, A. et al. Atomic-scale interface engineering of Majorana edge modes in a 2D magnet-superconductor hybrid system. *Sci. Adv.* **5**, eaav6600 (2019).
- 26 Abrikosov, A.A. Nobel Lecture: Type-II superconductors and the vortex lattice. *Rev. Mod. Phys.* **76**, 975-979 (2004).
- 27 Lounasmaa, O.V. & Thuneberg, E. Vortices in rotating superfluid 3He. *Proc. Natl. Acad. Sci. U. S. A* **96**, 7760-7767 (1999).
- 28 Blasuwgeers, R. et al. Double-quantum vortex in superfluid 3He-A. *Nature* **404**, 471-473 (2000).
- 29 Matsumura, H. et al. Large Reduction in the **a**-axis Knight Shift on UTe₂ with $T_c = 2.1$ K. *J. Phys. Soc. Jpn.* **92**, 063701 (2023).
- 30 Frank, C. E. et al. Orphan high field superconductivity in non-superconducting uranium ditelluride. *Nat. Commun.* **15**, 3378 (2024).
- 31 Gu, Q. et al. Pair wavefunction symmetry in UTe₂ from zero-energy surface state visualization. Preprint: arXiv.2501.16636
- 32 Wei, D.S., et al. Interplay between magnetism and superconductivity in UTe₂. *Phys. Rev. B* **105**, 024521 (2022).
- 33 Tokuyasu, T.A., Hess, D.W. & Sauls J.A. Vortex states in an unconventional superconductor and the mixed phases of UPt₃. *Phys. Rev. B* **41**, 8891-8903 (1989).
- 34 Ichioka, M. and Machida, K. Field dependence of the vortex structure in chiral *p*-wave superconductors. *Phys. Rev. B* **65**, 224517 (2002).
- 35 Sauls, J. A. & Eschrig, M. Vortices in chiral, spin-triplet superconductors and superfluids. *New. J. Phys.* **11**, 075008 (2009).
- 36 Lee, D. & Schnyer, A. P. Structure of vortex-bound states in spin-singlet chiral superconductors. *Phys. Rev. B* **93**, 064522 (2016).
- 37 Tanuma, Y., Hayashi, N., Tanaka, Y. & Golubov, A.A. Model for vortex-core tunneling spectroscopy of chiral *p*-wave superconductors via odd-frequency pairing states. *Phys. Rev. Lett.* **102**, 117003 (2009).
- 38 Ishizuka, J., Sumita, S., Daido, A., Yanase, Y. Insulator-Metal Transition and Topological Superconductivity in UTe₂ from a First-Principles Calculation. *Phys. Rev. Lett.* **123**, 217001 (2019).
- 39 Kinjo, K., et al. Change of superconducting character in UTe₂ induced by magnetic field. *Phys. Rev. B* **107**, L060502 (2023).
- 40 Ikegaya, S. et al. Identification of spin-triplet superconductivity through a helical-chiral phase transition in Sr₂RuO₄ thin films. *Phys. Rev. B* **101**, 220501 (2020).
- 41 Krishana, K., Ong, N. P., Li, Q., Gu, G. D. & Koshizuka, N. Plateaus observed in the field profile of thermal conductivity in the superconductor Bi₂Sr₂CaCu₂O₈. *Science* **277**, 83-85 (1997).
- 42 Takamatsu, S. & Yanase, Y. Spin-triplet pairing state of Sr₂RuO₄ in the *c*-axis magnetic field. *J. Phys. Soc. Jpn.* **82**, 063706 (2013).

-
- 43 Kitagawa, S. et al. Clear Reduction in Spin Susceptibility and Superconducting Spin Rotation for H parallel a in the Early-Stage Sample of Spin-Triplet Superconductor UTe₂. *J. Phys. Soc. Jpn.* **93**, 123701 (2024).
- 44 Lee, S. Anisotropic field-induced changes in the superconducting order parameter of UTe₂. Preprint: arXiv:2310.04938.
- 45 Chen, X. et al. Observation and characterization of the zero energy conductance peak in the vortex core state of FeTe_{0.55}Se_{0.45}. Preprint: arXiv:1909.01686.
- 46 Schnyder, A.P. & Brydon, P.M.R. Topological surface states in nodal superconductors. *J. Phys.: Condens. Matter* **27**, 243201 (2015).
- 47 Tsutsumi, Y., Kawakami, T., Shiozaki, K., Sato, M. & Machida, K. Symmetry-protected vortex bound state in superfluid ³He-B phase. *Phys. Rev. B* **91**, 144504 (2015).
- 48 Sakurai, J.J. & Napolitano, Modern Quantum Mechanics, 2nd Edition. Addison-Wesley (2011).
- 49 Kim, H., Nagai, Y., Rózsa, L., Schreyer, D., Wiesendanger, R. Anisotropic non-split zero-energy vortex bound states in a conventional superconductor. *Appl. Phys. Rev.* **8**, 031417 (2021).
- 50 Kitaev, A. Unpaired Majorana fermions in quantum wires. *Phys. Uspekhi* **44**, 131–136 (2001).
- 51 Eskildsen, M.R. Vortex Imaging in the pi Band of Magnesium Diboride. *Phys. Rev. Lett.* **89**, 187003 (2002).
- 52 Aishwarya, A. et al. Magnetic-field-sensitive charge density waves in the superconductor UTe₂. *Nature* **618**, 928–933 (2023).
- 53 Kengle, C.S. et al. Absence of bulk charge density wave order in the normal state of UTe₂. *Nat. Commun.* **15**, 9713 (2024).
- 54 Kogan, V.G. & Zhelezina, N.V. Field dependence of the vortex core size. *Phys. Rev. B* **71**, 134505 (2005).
- 55 Tao, R. et al. Direct visualization of the nematic superconductivity in Cu_xBi₂Se₃. *Phys. Rev. X* **8**, 041024 (2018).
- 56 Liu, X., Chong, Y. X., Sharma, R. & Davis, J. C. S. Atomic-scale visualization of electron fluid flow. *Nat. Mater.* **20**, 1480–1484 (2021).
- 57 Anthore, A., Pothier, H. & Esteve, D. Density of States in a Superconductor Carrying a Supercurrent. *Phys. Rev. Lett.* **90**, 127001 (2003).
- 58 Silaev, M.A., Thuneberg, E.V., Fogelström, M. Lifshitz transition in the double-core vortex in ³He-B. *Phys. Rev. Lett.* **115**, 235301 (2015).
- 59 Tsutsumi, Y. & Machida K. Topological spin texture and d-vector rotation in spin-triplet superconductors: A case of UTe₂. *Phys. Rev. B* **110**, L060507 (2024).
- 60 Iguchi, Y. et al. Microscopic imaging homogeneous and single phase superfluid density in UTe₂. *Phys. Rev. Lett.* **130**, 196003 (2023).
- 61 Glusevich, N. & Sauls, J. A. Kibble-Zurek Dynamics & Statistics of Topological Defects in Chiral Superfluid ³He Films. Preprint: arXiv:2412.03544
- 62 Berlinsky, A. J., Fetter, A. L., Franz, M., Kallin, C. & P. I. Soininen. Ginzburg-Landau theory of vortices in d-wave superconductors. *Phys. Rev. Lett.* **75**, 2200–2203 (1995).
- 63 Zhang, P. et al. A precise method for visualizing dispersive features in image plots. *Rev. Sci. Instrum.* **82**, 043712 (2011).
- 64 Deng, H. et al. Chiral kagome superconductivity modulations with residual Fermi arcs. *Nature* **632**, 775–781 (2024).

-
- 65 Chen, M. et al. Discrete energy levels of Caroli-de Gennes-Matricon states in quantum limit in $\text{FeTe}_{0.55}\text{Se}_{0.45}$. *Nat. Commun.* **9**, 970 (2018).
- 66 Lin, M. et al. Low Energy Band Structure and Symmetries of UTe_2 from Angle-Resolved Photoemission Spectroscopy. *Phys. Rev. Lett.* **124**, 076401 (2020).